文章编号： 1007-8827(2020)04-0358-13

锂离子电池用 $CoMoO_4$/炭颗粒与氮掺杂多孔炭复合材料

朱玉龙， 王宜先， 高 才， 赵伟楠， 王晓波， 吴明铂
(中国石油大学(华东)新能源学院,化学工程学院,重质油国家重点实验室, 山东 青岛 266580)

摘 要： 超精细过渡金属氧化物(TMO)在储锂方面具有巨大潜力,但在实际应用中还存在易团聚、电导率低等挑战。本文采用双炭复合方法,首先将 ZIFs-67 固定于模板法制备的石油沥青基多孔炭骨架上,然后将配位 Co^{2+} 原位转化为 $CoMoO_4$@炭纳米颗粒,生成 $CoMoO_4$@炭纳米颗粒/多孔炭骨架($CoMoO_4$@CP/CF)。通过 ZIFs-67 热解制备出 N 掺杂炭骨架,从本质上提高 $CoMoO_4$ 电子传输能力,而超细炭纳米颗粒可以有效阻止 $CoMoO_4$ 聚集。基于上述优点,将该复合材料用做锂离子电池负极,电流密度为 1 A g^{-1} 时,可提供高达 818 mAh g^{-1} 的可逆比容量。该合成方法为高性能储能电极材料的设计提供了新途径。

关键词： $CoMoO_4$;多孔炭;N 掺杂;负极;锂离子电池
中图分类号： TB33 **文献标识码：** A

基金项目:国家自然科学基金(51572296, U1662113);中央高校基本科研基金(15CX08005A);中国石油天然气股份有限公司科学研究与技术开发项目(2016B-2004(GF)).

通讯作者:吴明铂,博士. E-mail: wumb@upc.edu.cn
作者简介:朱玉龙,硕士研究生. E-mail: 245830503@qq.com

$CoMoO_4$ -N-doped carbon hybrid nanoparticles loaded on a petroleum asphalt-based porous carbon for lithium storage

ZHU Yu-long, WANG Yi-xian, GAO Cai, ZHAO Wei-nan, WANG Xiao-bo, WU Ming-bo
(*State Key Laboratory of Heavy Oil Processing, College of New Energy, College of Chemical Engineering, China University of Petroleum (East China), Qingdao* 266580, *China*)

Abstract: Ultrafine transition metal oxides have great potential for efficient lithium storage but some key problems, such as a strong tendency to aggregate and poor electrical conductivity, need to be solved for their possible application. Here, hybrid nanoparticles of $CoMoO_4$ and N-doped carbon were formed in a petroleum asphalt-based porous carbon prepared by a template method. A Co-based zeolitic imidazolate framework (ZIF-67) was then synthesized in-situ in its pores from $Co(NO_3)_2 \cdot 6H_2O$ and 2-methylimidazole. The porous carbon was impregnated with $Na_2MoO_4 \cdot 2H_2O$ and polyvinyl pyrrolidone, followed by solvothermal treatment at 180 ℃ for 24 h and finally calcination to convert the loaded components into hybrid nanoparticles of $CoMoO_4$ and N-doped carbon. Results indicate that the N-doped carbon boosts the electron transport ability of $CoMoO_4$ and efficiently prevents its aggregation. At an optimal $CoMoO_4$ loading the composite was used as an anode material in a lithium ion battery and delivered a reversible specific capacity of 818 mAh g^{-1} at 1 A g^{-1}, an initial coulombic efficiency of around 70%, and outstanding cycle and structural stability during cycling. The strategy reported here may open up a new avenue for the rational design and construction of well-designed electrode materials for energy storage.

Key words: $CoMoO_4$; Porous carbon; N-doped; Anode; Lithium-ion battery

Received date: 2020-04-06; *Revised date*: 2020-07-08
Foundation item: National Natural Science Foundation of China (51572296, U1662113), Fundamental Research Funds for the Central Universities (15CX08005A), Financial Support from Taishan Scholar Project, Scientific Research and Technology Development Project of Petrochina Co., LTD (2016B-2004(GF)).

Corresponding author: WU Ming-bo, Ph. D, Professor. E-mail: wumb@upc.edu.cn
Author introduction: ZHU Yu-long, Master student. E-mail: 245830503@qq.com

English edition available online ScienceDirect(http://www.sciencedirect.com/science/journal/18725805).
Supplementary data associated with this article can be found in the online version.
DOI:10.1016/S1872-5805(20)60494-2

1 Introduction

The overuse of fossil fuels in past decades has aroused growing concerns about energy shortage and environment pollution[1-3]. The exploration of renewable and sustainable energy has been suggested as the most efficient technology to address these issues. Unlike the fossil fuels, these renewable sources are intermittent and the reliable use of them is in desperate need of robust energy storage systems. With the advantages of safety, high energy density, and excellent cycle stability[4-5], lithium ion batteries (LIBs) have been the dominating energy storage devices in today's market. However, the practical performance of the current LIBs can not meet the increasing demand of many current and emerging applications because of the limitations from the electrode materials. For example, the commercially available graphite anode has a low specific capacity and slow ion diffusion rate[6]. As a result, the searches for alternative anode materials with high specific capacity and fast ion diffusion rate are urgently required[7-12].

With the possibility of reacting reversibly with Li^+ ions, transition metal oxides (TMOs) afford a much higher theoretical capacity (600-1 000 mAh g^{-1}) than graphite anodes, thus attracting worldwide attention recently[12,13,44]. Previous researches indicate that the single metal oxides, such as Fe_3O_4, MoO_3, CuO, Co_3O_4, TiO_2 and SnO_2[13-19], usually suffer from pulverizations of primary particles, low initial coulombic efficiency (ICE) and poor cycling performance due to large volume expansion during lithiation/delithiation[20-22]. To address these issues, tremendous efforts have been devoted to mixed transition metal oxides (MTMOs) where the synergic effects rising from different metal elements can contribute to improved performance[23-24]. Typical examples include stannates, ferrites, cobaltates, nickelates and so on[25-28].

To further enhance the competitiveness of MTMOs, a myriad of modification strategies have been proposed, including construction of ultrafine particles as well as hybridization with nanocarbons[29-31]. Among them, $CoMoO_4$ has been widely used as electrode materials for LIBs owing to its high theoretical capacity (980 mAh g^{-1}) and feasible oxidation state, such as $CoMoO_4/Fe_2O_3$ core-shell nanorods[32], hierarchical $CoMoO_4$[33], fully conversion of MoO_3 by the introduction of $CoMoO_4$[34]. However, $CoMoO_4$ still suffers from low conductivity and particle aggregation. Through rationally hybridizing with porous carbon frameworks and/or optimizing the particle size of $CoMoO_4$, these drawbacks can be essentially overcome.

Hybrid structured $CoMoO_4$-carbon materials, such as $CoMoO_4$ nanorods-graphene[35], $CoMoO_4$@Co_3O_4 on flexible carbon fabric[24], electrospun lotus root-like $CoMoO_4$@ graphene nanofibers[36], coaxial $CoMoO_4$ nanowire on carbon cloth[49], have been reported with improved lithium storage performance. On the one hand, the reduced particle size can contribute to a shortened Li^+ ion diffusion length. On the other hand, loading the ultrafine $CoMoO_4$ on conductive carbon particles can improve the local electron transport rate. Zeolitic imidazolate framework (ZIF) is a branch of metal organic frameworks (MOFs) which consists of metal ions or clusters combined with organic linkers/ligands through strong coordination bonds. Meanwhile, ZIFs are thought to be desired porous carbon precursors[37-38]. Furthermore, imidazoles in ZIFs can provide N heteroatom-doping owing to its high nitrogen content, which improves electron conductivity by modifying electron density[39-40].

Petroleum asphalt, as a residual product in processing of crude oil, has been used in water-proofing, paving roads or fuels for quite a few years[27,40]. Nevertheless, these applications are still of low value and how to realize its value-added utilization is meritorious. Taking this into consideration, asphalt is promising to serve as anode precursors of LIBs and electrode materials of supercapacitors because it is abundant in aromatic ring and available in massive production. Though a lot of work has been done to realize this goal, asphalt based carbon materials still have room for improvement[40-42].

Herein, we report the dual carbon hybridizing technology to fabricate ultrafine MTMO, namely $CoMoO_4$, and carbon composites for robust lithium storage. Starting from 3D asphalt-derived porous carbon framework, ZIF-67 nanoparticles are firstly loaded on the carbon frameworks with the help of oxygen containing functional groups, such as —OH, —COOH. Because of the different diffusion rates of metal ion in a mixed solvent, the coordinative Co^{2+} in-situ has metal ion exchange reaction with MoO_4^{2-} to convert into ultrafine $CoMoO_4$ @ carbon nanoparticles loaded on carbon framework. The ultrafine $CoMoO_4$ is firstly embedded into the ZIF-derived carbon nanoparticles to prevent the tendency of $CoMoO_4$ aggregation. The 3D porous carbon framework can secure the efficient electron transfer. When evaluated as anode materials for LIBs, such a nanohybrid delivers a reversible specific capacity of 818 mAh g^{-1} and long-term stability of over 450 cycles.

2 Experimental

2.1 Chemicals

Petroleum asphalt was obtained from China National Petroleum Corporation. 20 nm γ-Fe_2O_3 nanoparticles was purchased from Macklin Biochemical Co., Ltd. HCl (36 wt.%-38 wt.%) was purchased from Sinopharm Chemical Reagent Co., Ltd. Co $(NO_3)_2 \cdot 6H_2O$ (99 wt.%), $Na_2MoO_4 \cdot 2H_2O$ (99 wt.%), polyvinyl pyrrolidone (PVP, average MW 58000, K29-32) and 2-methylimidazole (98 wt.%) were purchased from Aladdin Industrial Corporation. All chemicals were directly used without further purification.

2.2 Synthesis

2.2.1 Synthesis of 3D carbon framework (CF)

The 3D carbon framework was prepared according to our previous work[40]. 50 g of petroleum asphalt was loaded in a 100 mL high-pressure autoclave for thermal pre-treatment at 380 ℃ for 14 h in nitrogen atmosphere. The pre-treated petroleum asphalt was collected after cooling down to room temperature naturally. Subsequently, 2 g of pre-treated product was dissolved in 80 mL toluene. Then 6 g of γ-Fe_2O_3 nanoparticles were added into the aforementioned solution. After that, the solvent was fully evaporated and the as-obtained mixture was carbonized at 800 ℃ for 1 h under N_2 atmosphere with a heating rate of 5 ℃/min . Finally, the obtained black powder was then washed with 4 mol/L HCl and deionized water sequentially before drying at 60 ℃ overnight. Then as-prepared product was denoted as carbon framework (CF).

2.2.2 Preparation of $CoMoO_4$@CP/CF

Firstly, 0.2 g of CF was added into a mixture of 15 mL methanol and 15 mL isopropanol under stirring followed by sonication for 15 min. Next, 1 mmol $Co(NO_3)_2 \cdot 6H_2O$ was dispersed in above mixture (denoted as solution A). Then, 2 g of 2-methylimidazole was dissolved in a mixture (denoted as solution B) of 5 mL methanol and 5 mL isopropanol followed by sonication for 10 min. Solution B was poured into solution A and mixed thoroughly by vigorous stirring. Finally, 1 mmol $Na_2MoO_4 \cdot 2H_2O$ and 0.5 g of PVP were added to the resulting solution mixture before sonication for 30 min. The solution was vigorously stirred for 24 h. Then, the dispersion was transferred into a 50 mL Teflon-lined autoclave, heated to 180 ℃ and kept for 20 h. At last, the black powder was collected by centrifugation and dried in air overnight before calcination at 500 ℃ for 3 h under N_2 atmosphere with a heating rate of 2 ℃ min^{-1} (denoted as precursor of $CoMoO_4$@CP/CF). For comparison, CoO@CP/CF and $CoMoO_4$/CF were prepared using a similar procedure without adding $Na_2MoO_4 \cdot 2H_2O$ and 2-methylimidazol, respectively.

In addition, the sample was also calcinated at different temperatures (400, 500, 600 ℃, and denoted respectively as 400, 500, 600) to investigate the effect of temperature on the material. After exposed in air for several days, the precursor of $CoMoO_4$@CP/CF was further calcinated at 400 ℃ with a heating rate of 3 ℃ min^{-1} under N_2 atmosphere (denoted as $CoMoO_4$@CP/CF). The precursor of $CoMoO_4$@CP/CF was also further calcinated at 300 and 400 ℃ for 3 h with a heating rate of 3 ℃ min^{-1} in air (denoted as 500-300-Air, 500-400-Air). Besides, different mass loadings of $CoMoO_4$ on $CoMoO_4$@CP/CF were investigated by a similar preparation method except for adding 0.5 mmol $Co(NO_3)_2 \cdot 6H_2O$ and 0.5 mmol $Na_2MoO_4 \cdot 2H_2O$, and 2 mmol $Co(NO_3)_2 \cdot 6H_2O$ and 2 mmol $Na_2MoO_4 \cdot 2H_2O$, and denoted as 0.5-$CoMoO_4$@CP/CF and 2-$CoMoO_4$@CP/CF, respectively.

2.3 Characterization

The crystal structure of different samples was detected by X-ray diffraction (XRD, X´Pert PRO MPD) worked at 40 kV and 40 mA (Cu $K\alpha$, λ = 0.154 066 nm). Morphologies of the as-made samples were obtained by field emission scanning electron microscopy (FESEM, Hitachi S-4800). Transmission electron microscopy (TEM), energy dispersive spectroscopy (EDS), and selected area electron diffraction (SAED) were tested on a JEM-2010 system at 220 kV. The specific surface area and pore structure were investigated by nitrogen sorption (Micromeritics, ASAP2020, America). Raman spectra were tested on a Jobine Yvon Labram-010 Raman spectrometer. X-ray photoelectron spectroscopy (XPS) analyses were carried out on a PHI 5 000 VersaProbe instrument (ULVAC-PHI, Japan).

2.4 Electrochemical measurements

The as-made material (70 wt%), acetylene black (20 wt%), binder (CMC, 10 wt%) were mixed and dispersed in N-methyl-2-pyrrolidinone. Then, the slurry was coated on the copper foil and dried at 80 ℃ for 12 h in a vacuum oven. The mass loading of each electrode was 1.1-1.2 mg cm^{-2}. Then, CR2032 coin type half cells were assembled in an Ar-filled glove box, with Li foil as the counter and reference electrodes, Celgard 2400 film served as a separator, and 1mol/L $LiPF_6$ in (1∶1, *v*/*v*) ethylene carbonate and dimethyl carbonate (EC/DMC) as an electrolyte. The galvanostatic charge-discharge results were obtained on a Land CT2001A battery test system

under a potential range of 0.01-3V (vs. Li^+/Li). Cyclic voltammetry (CV) curves (scan rate: 0.2 mV s^{-1}) and electrochemical impedance spectra (EIS) at a frequency range of 100 kHz to 0.01 Hz with an AC amplitude of 5 mV were conducted on a CHI760E (CH Instruments, Shanghai, China) electrochemical workstation.

3 Results and discussion

Fig. 1 depicts the fabrication process of $CoMoO_4$@CP/CF. Firstly, 3D porous carbon framework was made according to our previous report[41]. What is worthy to mention is the use of γ-Fe_2O_3, as γ-Fe_2O_3 is magnetic which contributes to the formation of a connected porous carbon framework when the mixture is stirred with magneton, while α-Fe_2O_3 is non-magnetic. The formation of pores are caused by removal of γ-Fe_2O_3 template by strong acidic HCl. Then, ZIF-67 nanoparticles were loaded on these porous carbon frameworks with the help of oxygen containing functional groups, such as —OH, —COOH. The function of PVP mainly lies on controlling the particle size of ZIF-67 to prevent formation of bulky ZIF-67 particle. Finally, due to the faster diffusion rate of coordinative Co^{2+} and slower diffusion rate of MoO_4^{2-} in the mixed solvent, metal ion exchange reaction occurred. Thus, the ZIFs-67 mediated $CoMoO_4$ precursor was formed by a one-pot solvothermal method before being calcinated to obtain $CoMoO_4$@CP/CF.

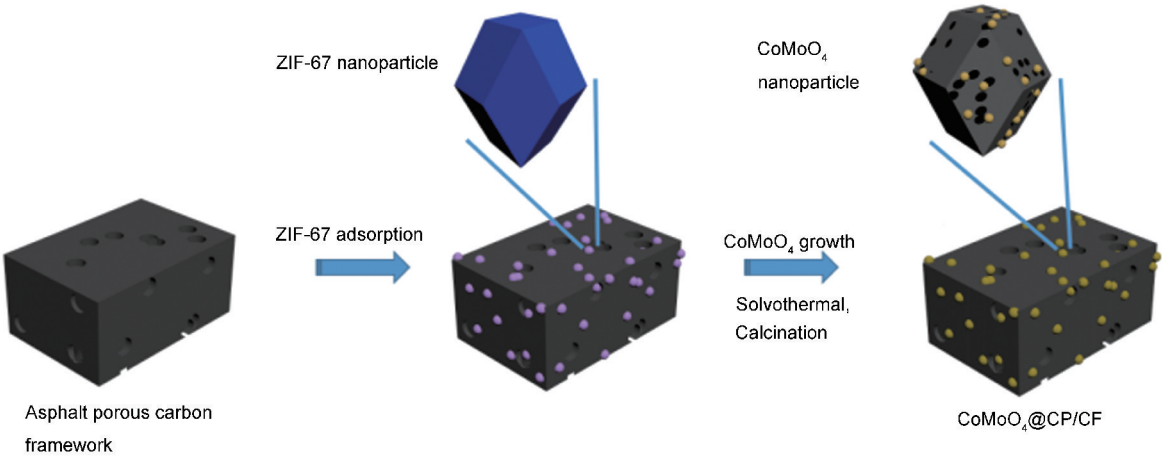

Fig. 1　Schematic illustration of the preparation process of $CoMoO_4$@CP/CF.

As shown in Fig. 2a, the XRD patterns of CoO@CP/CF and $CoMoO_4$@CP/CF show metal phases of materials. It can be seen that CoO@CP/CF has several peaks, which are well corresponding to CoO standard peaks and there is no other phase of Co metal observed. In terms of $CoMoO_4$@CP/CF, the sample was calcinated twice to improve the crystallinity of $CoMoO_4$. The main peaks of $CoMoO_4$@CP/CF correspond to standard $CoMoO_4$ and the peak with highest intensity fits standard $CoMoO_4$ very well. Besides, two weak peaks belonging to $CoMoO_3$ and Co_3C are also observed. This phenomenon is ascribed to the reduction reaction of metal oxides under carbon atmosphere.

In order to investigate temperature effect on the material, we also prepared samples at different calcinating temperatures which are shown in Fig. S1a. The pattern in the 400 sample which mainly contains MoO_3 is totally different from the 500 and 600 samples while the 500 and 600 samples are similar and have some metal phase of $CoMoO_4$ and some other impure metal phases of Co and Mo. This may be resulted from unsuccessful metal phase transformation under relative low temperature, so $CoMoO_4$ metal phase can not be formed. Fig. S1b shows two peaks of CF at 23.9° and 43.2°, which are ascribed to amorphous carbon and graphitic carbon, respectively[40]. Meanwhile, it proves that Fe_2O_3 has been removed because no peaks of Fe_2O_3 can be found. As shown in Fig. S2, we conducted XRD analysis of the precursors of $CoMoO_4$@CP/CF further calcinated in air for a better understanding of secondary calcination effect on the precursor. There is no obvious metal phase change when the precursor of $CoMoO_4$@CP/CF was calcinated once more at 300 ℃ in air, whereas, a high purity metal phase of $CoMoO_4$ was formed when the precursor of $CoMoO_4$@CP/CF was calcinated at 400 ℃ in air. And the XRD result of $CoMoO_4$@CP/CF calcinated twice at 400 ℃ in N_2 atmosphere matches well with that of $CoMoO_4$/CF. This phenomenon confirms that a second thermal treatment at 400 ℃ is favorable for the phase transformation of precursor while it is not at 300 ℃. While the precursor of $CoMoO_4$@CP/CF was exposed to air

for several days to adsorb enough oxygen and then further calcinated at 400 ℃ under N_2 atmosphere to prevent the carbon element of $CoMoO_4$@CP/CF from losing when it was calcinated in air.

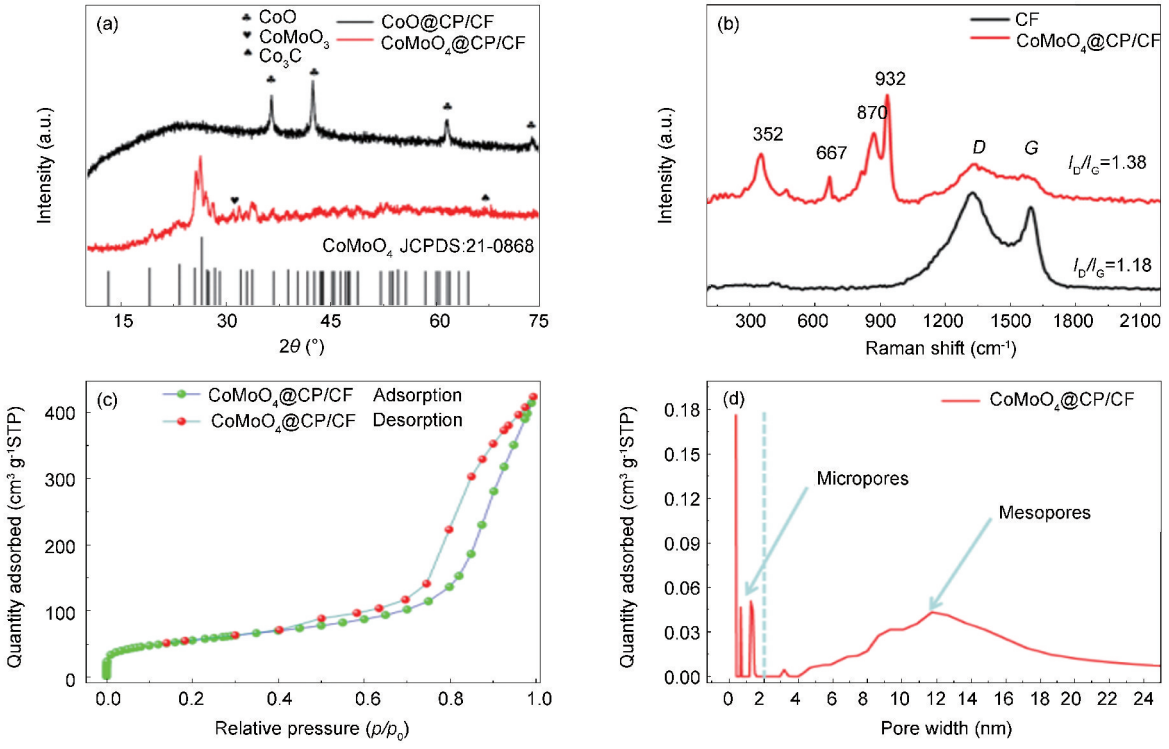

Fig. 2 (a) XRD patterns, (b) Raman spectra, (c) nitrogen adsorption-desorption isotherms and (d) pore size distribution of $CoMoO_4$@CP/CF.

Raman spectra are shown in Fig. 2b. In view of $CoMoO_4$@CP/CF, peaks observed at 352, 667, 870, 932 cm^{-1} are ascribed to $CoMoO_4$, and this result agrees well with the XRD analysis[36]. Besides, *D* band (1 356 cm^{-1}) from structural defects and *G* band (1 596 cm^{-1}) from the vibration of sp^2-bonded graphitic carbon atoms can be seen in the Raman spectra[10]. $CoMoO_4$@CP/CF shows a larger I_D/I_G ratio than that of CF, because further calcination can provide more defects which are essential for carbon-based electrodes. Additionally, pore structure was investigated by nitrogen adsorption. In Fig. 2c, a typical type-IV isotherm of $CoMoO_4$@CP/CF with an apparent hysteresis loop is clearly obtained. The $CoMoO_4$@CP/CF has a BET surface area of 196.6 $m^2\ g^{-1}$ and this relatively smaller specific surface area may be resulted from ultrafine carbon nanoparticles formed in pyrolysis of ZIFs covering on the pores of substrate CF. Micropores and mesopores dominated pore size distribution of $CoMoO_4$@CP/CF is shown in Fig. 2d. Micropores and mesopores are clearly observed in the pore width distribution curve. This hierarchical pore structure plays a key role in offering more active sites and reservoirs for Li^+ storage. The $CoMoO_4$@CP/CF delivered an average pore size of 13.12 nm. A part of mesopores are a little bit smaller than the template because micropores originated from ZIFs cover on/in mesopores. Some mesopores are bigger than the template because of the aggregation of the template.

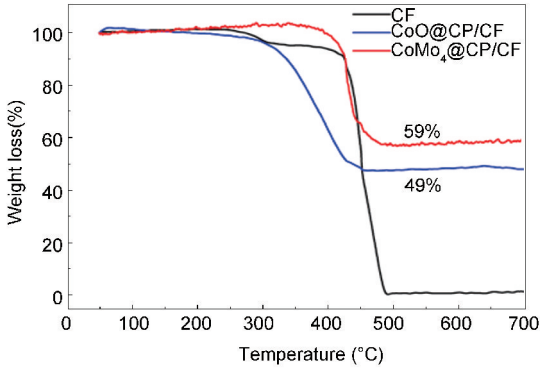

Fig. 3 Thermogravimetric curves of CF, CoO@CP/CF and $CoMoO_4$@CP/CF.

In the Fig. 3, thermogravimetric analysis was applied to measure the metal content of $CoMoO_4$@CP/CF and CoO@CP/CF after oxidation at 800 ℃ in air with a heating rate of 5 ℃/min. As shown, the thermogravimetric curve of CF indicates that they start to lose weight starts at 290 ℃ and the weight loss stop at 490 ℃. This may be resulted mainly from the carbon loss in the form of CO_2. The $CoMoO_4$@CP/CF has a 78% residue derived from $CoMoO_4$, and CoO@CP/CF has a 59% residue of CoO.

The morphology and structure were investigated by scanning electron microscopy (SEM) and transmission electron microscopy (TEM). As the SEM images of ZIF-67/CF shown in Fig. S3, ZIF-67 anchored on CF is in a standard octahedron shape. In addition, numerous pores are visible in SEM images of CF (Fig. S4a) due to the removal of the template. When CF is combined with ZIFs-67 followed by calcination, we can see a lot of linked nanoparticles anchored on CF and the pore structure of CF is hardly observed in the SEM image of CoO@CP/CF. Furthermore, interconnection of ZIFs is clearly seen due to the formation of strong coordination bonds between metal ions and organic linkers (Fig. S4b). In the SEM images of $CoMoO_4$@CP/CF (Fig. 4a-c), it is obvious that the mass loading of $CoMoO_4$ increases with the amounts of cobalt salt and molybdenum salt. No aggregation phenomenon is detected, at the same time, pores and nanoparticles can be clearly seen. This uniform distribution of $CoMoO_4$ nanoparticles contributes greatly to the well electrochemical performance because of its abundant active sites. Besides, the TEM images of CF also prove that pores are formed after the removal of the template (Fig. S4c and S4d).

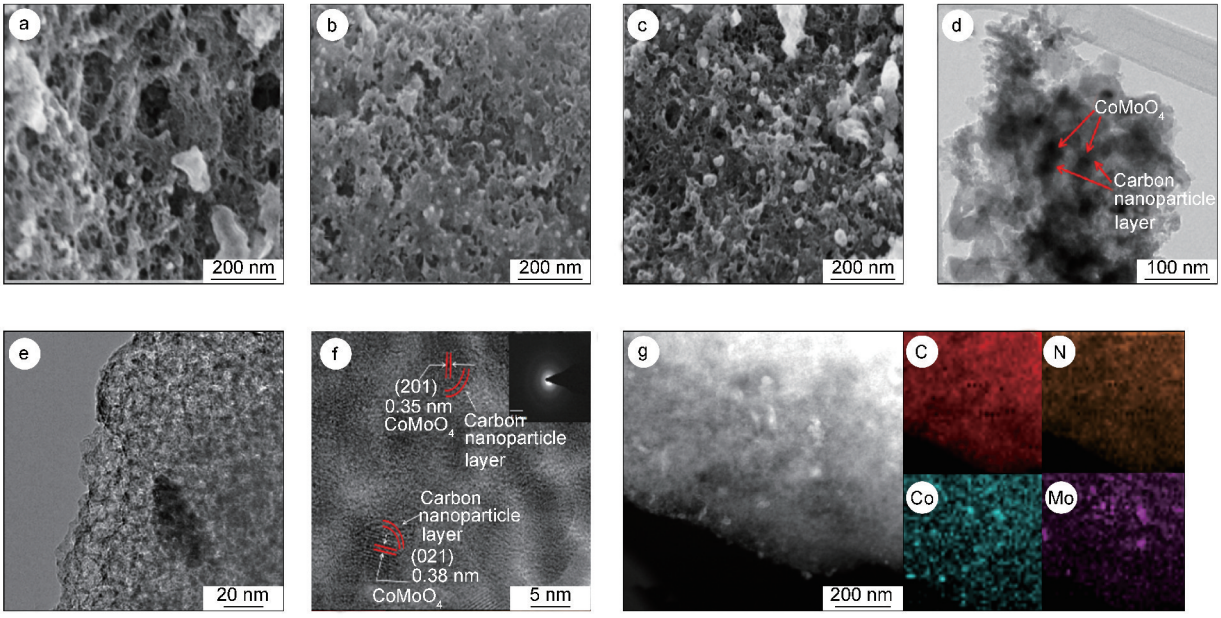

Fig. 4　SEM images of (a) 0.5-$CoMoO_4$@CP/CF, (b) $CoMoO_4$@CP/CF, (c) 2-$CoMoO_4$@CP/CF, (d-f) TEM images and high-magnification TEM image of $CoMoO_4$@CP/CF and (g) TEM image of $CoMoO_4$@CP/CF and the corresponding elemental mappings of C, N, Co and Mo.

However, less pores are seen in TEM images of $CoMoO_4$@CP/CF (Fig. 4d, 4e). This phenomenon may be resulted from Co^{2+} linked by the micropores-dominated ZIFs and carbon nanoparticles coated on the surface of CF network. In further analysis, TEM image of $CoMoO_4$@CP/CF shows smaller $CoMoO_4$ clusters successfully anchored in the carbon framework, which are presented in the form of dark pots, and carbon nanoparticle layer surrounded $CoMoO_4$ clusters are clearly observed (Fig. 4d). HRTEM of $CoMoO_4$@CP/CF clearly shows the crystal lattice of $CoMoO_4$ clusters with a size of 5-10 nm and this is similar to Yao's work[44] (Fig. 4f). The lattice fringe is around 0.38 nm and 0.35 nm, corresponding to the spacing of (021) and (201) planes of $CoMoO_4$. SAED result with a ring pattern shows low crystallinity due to ultrafine carbon nanoparticles derived from ZIFs surrounding around $CoMoO_4$ particles (inset of Fig. 4f). Meanwhile, elemental mapping analyses are carried out to demonstrate element dispersion, and we can clearly see that C, N, Co and Mo elements are dispersed uniformly in $CoMoO_4$@CP/CF.

X-ray photoelectron spectroscopy (XPS) is also used to further investigate elemental components of

samples. Fig. 5a clearly shows the presence of C, N, O, Co and Mo elements in $CoMoO_4$@CP/CF, but only C and O elements exist in CF. This result well proves that compounds containing Co, Mo, N grow on CF network. In comparison, only Co element is obtained in the sample of CoO@CP/CF, which agrees well with the XRD result. The high-resolution C 1s of $CoMoO_4$@CP/CF indicates some functional groups (—OH, —COOH) on CF, which may help $CoMoO_4$ grow on carbon network due to hydrogen bonding or van der Wall's intercalation (Fig. S5)[44]. The peaks centered at 232.5 and 235.5 eV belong to Mo $3d_{5/2}$ and Mo $3d_{3/2}$ of Mo^{6+}, respectively, which demonstrate the existence of MoO_4^{2-} (Fig. 5b)[45].

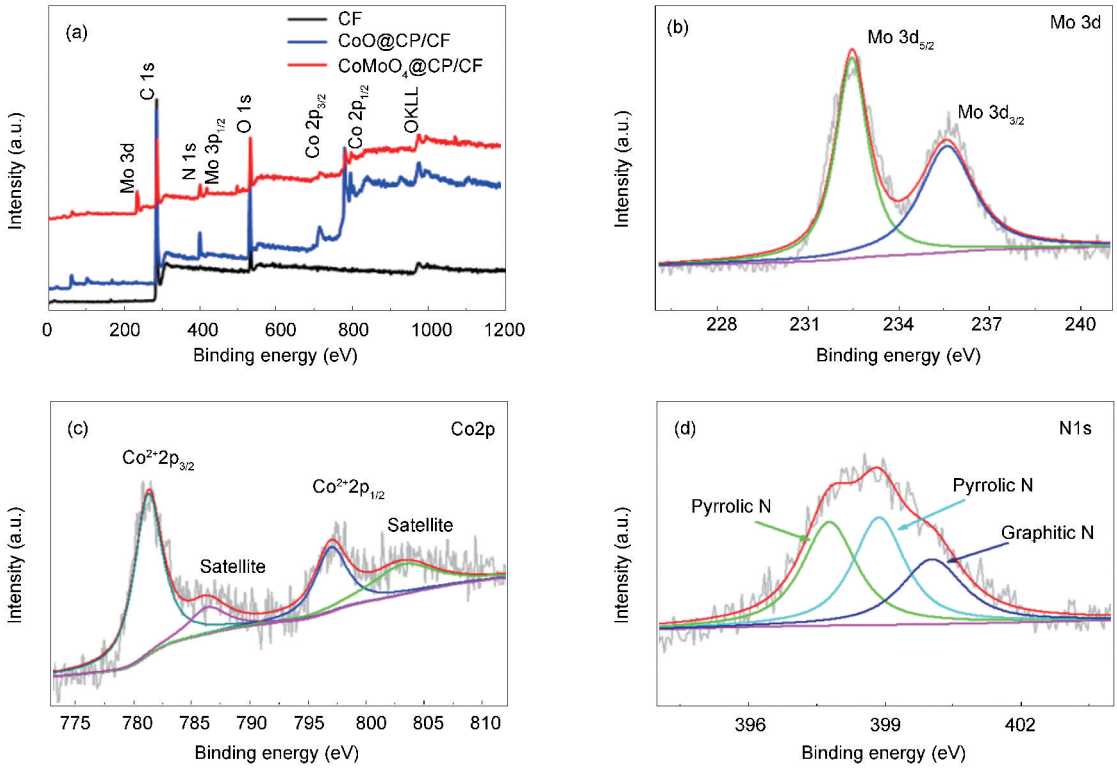

Fig. 5 XPS spectra of (a) CF, CoO@CP/CF, $CoMoO_4$@CP/CF, (b) Mo 3d spectrum, (c) Co 2p spectrum and (d) N 1s spectrum of $CoMoO_4$@CP/CF.

In terms of Co^{2+} spectrum, peaks at 781.3 and 797.0 eV originate from Co^{2+} $2p_{3/2}$ and Co^{2+} $2p_{1/2}$, respectively. The other two satellite peaks (at 786.3, 803.2 eV) are shakeup-type peaks of Co at the high binding energy side of the Co $2p_{3/2}$ and Co $2p_{1/2}$ edges (Fig. 5c)[46-47]. The N 1s peak can be divided into three types of N element, including pyridinic N, pyrrolic N and graphitic N (Fig. 5d)[37]. Especially, the existence of graphitic N is favorable for electrode materials because of it can tune the electronic properties and improve electronic conductivity of carbon[48]. In addition, element concentrations are also characterized in Table 1. The concentration of N element is obviously increased by introducing ZIFs and the percentages of Co (1.87%) and Mo (2.33%) demonstrate the metal content of $CoMoO_4$@CP/CF in detail. For the ratio of Co and Mo atoms (0.8) is close to the stoichiometry of $CoMoO_4$. The result is in accordance with the XRD pattern and Raman result, which show strong crystallinity of $CoMoO_4$.

Table 1 Elemental contents and concentrations of nitrogen species in CF, CoO@CP/CF and $CoMoO_4$@CP/CF analyzed by XPS measurements.

	C(at.%)	N(at.%)	O(at.%)	Co(at.%)	Mo(at.%)	Pyrrolic N(%)	Piridinic N(%)	Graphitic N(%)
$CoMoO_4$@CP/CF	54.08	8.53	25.19	5.87	6.33	36.83	36.64	26.52
CoO@CP/CF	71.06	8.79	14.86	5.29	/	58.78	23.16	18.06
CF	91.09	0.37	8.54	/	/	/	/	/

Electrochemical properties of as-made materials were investigated by assembling 2032 coin-type half

cells with Li metal. It is implied that the reaction mechanism can be followed by several equations[44,49]:

$$CoMoO_4 + 8Li^+ + 8e^- \longrightarrow Co + Mo + 4Li_2O \quad (1)$$

$$Co + Li_2O \longleftrightarrow CoO + 2Li^+ + 2e^- \quad (2)$$

$$Mo + 3Li_2O \longleftrightarrow MoO_3 + 6Li^+ + 6e^- \quad (3)$$

$$C\ (\text{porous carbon}) + xLi^+ + xe^- \longleftrightarrow Li_xC \quad (4)$$

Fig. 6a depicts the CV curve of $CoMoO_4$@CP/CF. Three peaks (at 0.15, 1.68 and 2.0 V) are observed in the first cathodic scan. Two sharp peaks at 1.68 and 2.0 V belonging to decomposition of $CoMoO_4$ in the first cathodic scan prove that $CoMoO_4$ exists in $CoMoO_4$@CP/CF. The peak at 0.15 V may come from the formation of solid electrolyte interphase (SEI)[44,49,51,53]. In the subsequent cycles, peaks centered at 0.6 and 1.43 V correspond to destruction of the crystal structure of $CoMoO_4$ accompanied with complete reduction to Co^0 and Mo^0[36]. For the first anodic scan of $CoMoO_4$ @ CP/CF, three peaks (at 1.27, 1.82 and 2.40 V) are observed. A broad weak peak at 1.27 V and an obvious peak at 1.82 V belong to the oxidation of Mo to Mo^{4+} and Co to Co^{2+}, respectively, while the peak at 2.40 V may correspond to Li^+ extraction from interfacial storage sites[50]. In the subsequent cycles, nearly overlapped curves prove that the reaction is highly reversible. The peak at 2.40 V disappears and the peaks centered at 1.36 V and 1.82 V correspond to the reactions in the eq (2) and eq (3), respectively, which prove that the reaction is fully reversible. All above prove that $CoMoO_4$ is successfully formed in $CoMoO_4$ @ CP/CF[44,52].

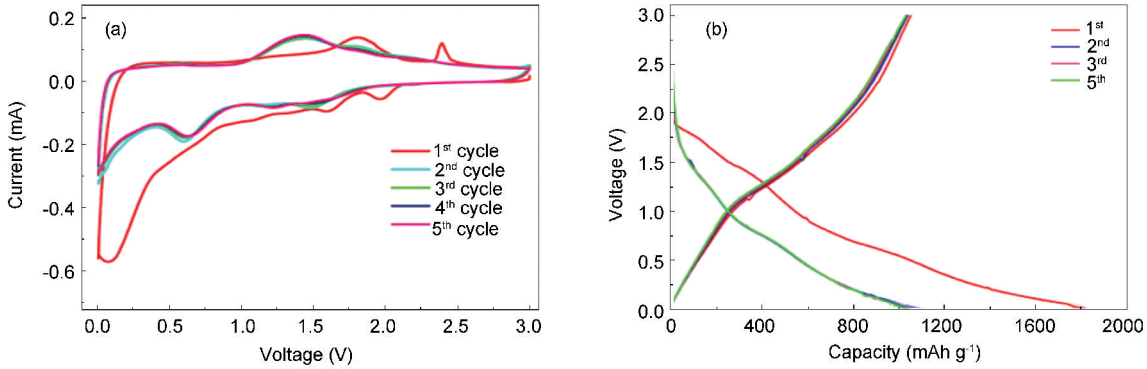

Fig. 6 (a) CV curves at a scan rate of 0.2 mV s^{-1} for $CoMoO_4$@CP/CF and (b) galvanostatic charge and discharge profiles at a current density of 100 mA g^{-1} for $CoMoO_4$@CP/CF.

In addition, discharge/charge and voltage curves of $CoMoO_4$@CP/CF were obtained by galvanostatic tests in Fig. 6b. The test was carried out at a current density of 100 mA g^{-1} between a voltage range of 0.01-3 V vs. Li^+/Li. For the first charge/discharge process of $CoMoO_4$@CP/CF, it has a discharge capacity of 1 838 mAh g^{-1} and a charge capacity of 1 050 mAh g^{-1} in the first cycle. Moreover, two voltage plateaus (1.68 V and 2.0 V) in the first discharge process and 1.27 V in the first charge process are in accordance with the corresponding CV curves. In the subsequent charge/discharge plots, well overlapped curves demonstrate a high reversibility of reactions.

The cyclability and rate performance of as-made materials were further investigated. Fig. 7a depicts cycling performances of CF, CoO@CP/CF and $CoMoO_4$@CP/CF while $CoMoO_4$@CP/CF exhibits the highest specific capacity of 818 mAh g^{-1} after cycling for 450 times. As shown, there is an obvious tendency of going up for both CoO@CP/CF and $CoMoO_4$ @CP/CF which may be caused by the activation process of electrode materials in the initial tens of cycles. After that, reversible capacities of CoO@CP/CF and $CoMoO_4$@CP/CF tend to drop resulting from SEI film formation and irreversible "dead Li" formation. Moreover, the fluctuation of $CoMoO_4$@CP/CF may come from the partially ununiform dispersion of metal clusters. Remarkably, the specific capacity of $CoMoO_4$@CP/CF climbs up to ~818 mAh g^{-1} after reaching a capacity valley of ~635 mAh g^{-1}. Since the 200th cycle, the capacity of $CoMoO_4$ @CP/CF maintains at 818 mAh g^{-1} over 450 cycles with a capacity retention rate of 74%. In detail, this phenomenon may be originated from the reversible growth of a polymeric gel-like film resulting from kinetically activated electrolyte degradation with the increase of cycling numbers[54-58]. The going down and up feature is pretty common in petroleum-based carbon materials due to the gradual activation process, more specifically, more and more electrolyte goes into interlayers of active materials. The same phenomenon is observed in samples of CoO@CP/CF and CF, since carbon framework is involved in all of them. Meanwhile, CE

of $CoMoO_4$@CP/CF is also presented. Remarkably, the initial CE of $CoMoO_4$@CP/CF is up to 70.3% while the first discharge capacity is 1 101 mAh g^{-1} and the first charge capacity is 774 mAh g^{-1}, which further proves a high reversibility of $CoMoO_4$@CP/CF. For CoO@CP/CF, the material delivers a reversible of specific capacity of 530 mAh g^{-1} over 450 cycles with a capacity retention rate of 71%, and this inferior electrochemical performance may be ascribed to the low theoretical capacity of CoO (750 mAh g^{-1}). In the meantime, the cycling tendency of CoO@CP/CF also presents a minor upward trend caused by the activation process and a slow decay derived from the stable SEI film formation[58-59].

In view of the bare CF, CF exhibits a reversible specific capacity of 453 mAh g^{-1} with a capacity retention rate of 38%. The cycling trend of CF consists of two segments including a weak downward part and a upward part, which comes from a partial crystallinity degradation from graphitic carbon to a more disordered one after more active sites are exposed for lithium storage[10]. In addition, we also investigated the effect of temperature and other factors on cycling performance in Fig. S6. In the cycling performance curves of various thermal treatment process, we found that the first calcination temperature in 500 ℃ exhibits the best performance with a reversible capacity of 583 mAh g^{-1} and the capacity retention rate around 73% over 300 cycles. The sample 400 shows a specific capacity of 535 mAh g^{-1} with a capacity retention rate of 69% and the sample 600 affords a specific capacity of 558 mAh g^{-1} with a capacity retention rate of 71%. The similarity in different samples is attributed by the fact that carbon framework occupies remarkable ratio in as-made materials and dispersion of metal oxides may be un-uniform because pores on carbon framework are more or less uneven. Calcination temperature has a great influence on crystallinity degree of metal oxides and on carbonization of petroleum-based carbon materials. Additionally, we made a comparison of the electrochemical performances of previously reported $CoMoO_4$-based anode materials with our work in Table 2 and the as-made material exhibits a considerable long-cycle life with an excellent reversible specific capacity.

Table 2 Comparison of the electrochemical performances of previously reported $CoMoO_4$-based anode materials with our work.

Sample	Current density (mA g^{-1})	Cycle number (Times)	Reversible capacity (mAh g^{-1})	Journal	Ref.
$CoMoO_4$@CP/CF	1000	450	818		This work
$CoMoO_4$-G	100	40	968	Ionics	[35]
lotus like $CoMoO_4$/Graphene nanofiber	100	200	735	Electrochimica Acta	[36]
ultrathin $CoMoO_4$ on carbon fabric	100	150	1128	New J Chem	[24]
interconnected $CoMoO_4$	100	50	990±10	ACS AMI	[52]
$CoMoO_4/Co_4O_3$ hollow octahedrons	200	100	1050	Mater Chem A	[23]
hierarchically porous $CoMoO_4$	500	100	758	Nanoscale	[33]
$CoMoO_4/Fe_2O_3$ core-shell nanorods	500	80	990	J Alloys Compd	[32]
$CoMoO_4$ NP/rGO	740	600	620	ACS AMI	[44]
coxial $CoMoO_4$ nanowire on carbon cloth	1200	1000	764	Journal of Power Sources	[49]
	1000	100	875		
P-Mo-Co-HMs	1500	100	751	ACS Nano	[34]
	2000	587	587		

Fig. 7b shows the cycling performances of the $CoMoO_4$@CP/CF samples with different loadings of $CoMoO_4$. $CoMoO_4$@CP/CF gives the best result among these samples while 0.5-$CoMoO_4$@CP/CF has a 652 mAh g^{-1} reversible capacity with a capacity retention rate of 61.1%. However, 2-$CoMoO_4$@CP/CF suffers a severe drop during cycling and then increases to a capacity of 626 mAh g^{-1} with a capacity retention rate of 59.7%, which may be caused by activation process of massive transition metal oxides. Fig. 7c shows the rate performances of CF, CoO@CP/CF and $CoMoO_4$@CP/CF at current densities of 0.1, 0.2, 0.5, 1, 2 A g^{-1}. The $CoMoO_4$@CP/CF delivers reversible capacities of 1 035, 992, 828, 670, 415 mAh g^{-1}, CF delivers reversible capacities of 620, 551, 436, 322, 210 mAh g^{-1} and CoO@CP/CF presents reversible capacities of 633, 555, 396, 272, 159 mAh g^{-1} at 0.1, 0.2, 0.5, 1, 2 A g^{-1}, respectively. Especially, the as-made material of $CoMoO_4$@CP/CF can still maintain an initial capacity of 1 035 mAh g^{-1} after a higher current density of 2 A g^{-1} is suddenly switched to a lower density of

0.1 A g^{-1}, indicating that as-made material has a structural integrity and excellent reversibility at high current densities.

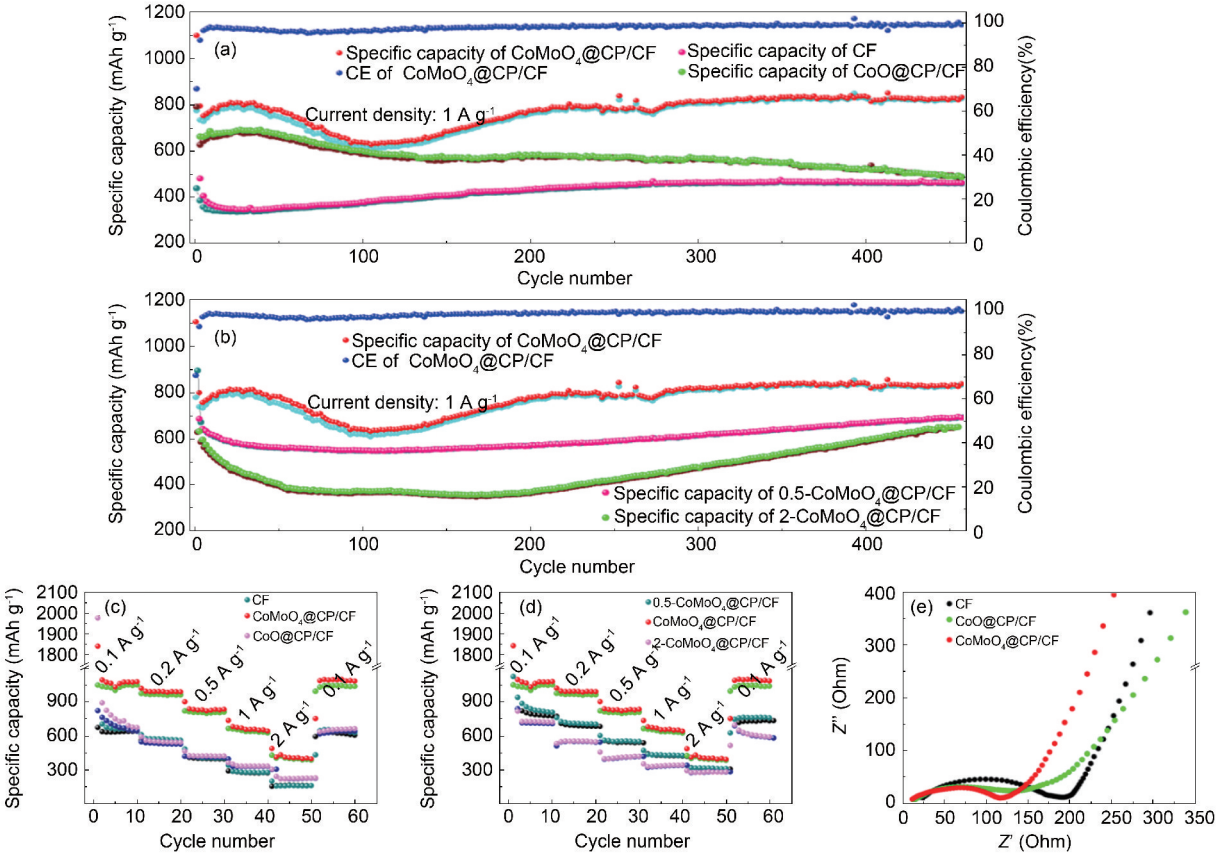

Fig. 7 (a) Cycling performances of CF, CoO@ CP/CF, $CoMoO_4$@ CP/CF and coulombic efficiency of $CoMoO_4$@ CP/CF, (b) cycling performances of 0.5-$CoMoO_4$@ CP/CF, $CoMoO_4$@ CP/CF, 2-$CoMoO_4$@ CP/CF, (c) rate performances of CF, CoO@ CP/CF and $CoMoO_4$@ CP/CF, (d) rate performances of 0.5-$CoMoO_4$@ CP/CF, $CoMoO_4$@ CP/CF, 2-$CoMoO_4$@ CP/CF and (e) electrochemical impedance spectra of CF, CoO@ CP/CF and $CoMoO_4$@ CP/CF.

In the Fig. 7d, it shows the rate performance of samples with different mass loadings of $CoMoO_4$. $CoMoO_4$@ CP/CF has the most appropriate loading compared with the other samples while 0.5-$CoMoO_4$ @ CP/CF delivers 783, 687, 544, 433, 315 mAh g^{-1} and 2-$CoMoO_4$ @ CP/CF presents 718, 552, 411, 339, 281 mAh g^{-1} at 0.1, 0.2, 0.5, 1, 2 A g^{-1}, respectively. Apart from the above electrochemical performance, electrochemical impedance spectroscopy was also applied to further explain the outstanding performance delivered by $CoMoO_4$ @ CP/CF. As shown in Fig. 7e, electrochemical impedance spectra consist of two parts: a semicircle in high frequency region which represents SEI film resistance and charge transfer resistance, and an upward slope line in low frequency region which represents Li^+ diffusion capability. In comparison of CF, CoO@ CP/CF and $CoMoO_4$@ CP/CF, $CoMoO_4$@ CP/CF has the lowest semicircle radius and highest slope indicating that $CoMoO_4$@ CP/CF possesses a superior electronic conductivity and fastest Li^+ diffusion ability among these samples[10,36]. This result is mainly attributed to carbon particles on the surface of $CoMoO_4$ that facilitate the electron transfer ability and Li^+ diffusion rate. At the same time, the N-doped carbon framework also gives a positive contribution to the electron transfer by tuning electronic property of carbon substrate.

The structural integrity of $CoMoO_4$ @ CP/CF electrode material was further investigated by SEM images before and after cycling at a current density of 1 A g^{-1}. Before cycling, a few $CoMoO_4$ particles are observed and other pieces of particles are ascribed to additives of acetylene black and CMC in Fig. S7a. The SEM image of $CoMoO_4$@ CP/CF electrode after cycling for 450 times is shown in Fig. S7b, it is found that an integrated porous carbon framework is clearly shown and a few $CoMoO_4$ particles exist in the porous carbon network. This phenomenon may be caused by transformation of crystalline $CoMoO_4$ particles to amorphous ones. In addition, there are a lot of pores which help store more Li^+ and no apparent cracking of the carbon framework is observed. Thus, the well retained structural integrity of the material en-

sures sufficiently favorable electrochemical performance of $CoMoO_4$@CP/CF during cycling.

4 Conclusion

A brand-new dual carbon hybridized $CoMoO_4$@CP/CF was prepared by a facile solvothermal reaction coupled with post calcination method. It has been demonstrated that ZIFs-67 is firstly anchored on carbon frameworks and then in-situ converted into $CoMoO_4$@CP/CF. Besides, N-doped carbon framework was realized with the introduction of imidazole to serve as N sources. The material performs a robust lithium storage competence: a considerable reversible capacity of 818 mAh g^{-1} at 1 A g^{-1}, a high ICE of 70.3% and a preferable rate capability of 1 035 mAh g^{-1} at 100 mA g^{-1}. Such a competitive lithium storage capability may be derived from a unique structure and excellent electron transport ability of ultrafine carbon nanoparticles and N-doped 3D carbon framework. This strategy provides a favorable approach for high value-added utilization of heavy oil for future energy storage materials.

References

[1] Wang H L, Zhu Q L, Zou R Q, et al. Metal-organic frameworks for energy applications[J]. Chem, 2017, 2(1): 52-80.

[2] Gao X L, Liu C X, Han G Y, et al. Reduced graphene oxide hydrogels prepared in the presence of phenol for high-performance electrochemical capacitors[J]. New Carbon Materials, 2019, 34(5): 403-416.

[3] Gao X L, Liu C X, Han G Y, et al. Reduced graphene oxide hydrogels prepared in the presence of phenol for high-performance electrochemical capacitors[J]. New Carbon Materials, 2019, 34(5): 403-416.

[4] Chen P, Ren H M, Yan L T, et al. Metal-organic frameworks enabled high-performance separators for safety-reinforced lithium ion battery[J]. ACS Sustainable Chemistry & Engineering, 2019, 7(19), 16612-16619.

[5] Yao Y, McDowell M T, Ryu I, et al. Interconnected silicon hollow nanospheres for lithium-ion battery anodes with long cycle life[J]. Nano Letters, 2011, 11(7), 2949-2954.

[6] Li X H, He Y B, Miao C, et al. Carbon coated porous tin peroxide/carbon composite electrode for lithium-ion batteries with excellent electrochemical properties[J]. Carbon, 2015, 81(1): 739-747.

[7] Ren D Z, Huang H, Qi J G, et al. One-pot template-free cross-linking synthesis of SiO_x-SnO_2@C hollow spheres as a high volumetric capacity anode for lithium-ion batteries[J]. Energy Technology, 2020, 2000314, 10.1002/ente.202000314.

[8] Yue X Y, Sun W, Zhang J, et al. Macro-mesoporous hollow carbon spheres as anodes for lithium-ion batteries with high rate capability and excellent cycling performance[J]. J Power Sources, 2016, 331: 10-15.

[9] Ren J, Ren R P, Lv Y K, et al. A flexible 3D graphene@CNT@MoS_2 hybrid foam anode for high-performance lithium-ion battery[J]. Chemical Engineering Journal 2018, 5(7):6343-6355.

[10] Wang Y X, Liu J Y, Pan L, et al. Preparation of carbon nanosheets from petroleum asphalt via recyclable molten-salt method for superior lithium and sodium storage[J]. Carbon, 2017, 122: 344-351.

[11] Kang B, Ceder G. Battery materials for ultrafast charging and discharging[J]. Nature, 2009, 458(7235): 190-193.

[12] Guo Y, Hu J, Wan L. Tin-nanoparticles encapsulated in elastic hollow carbon spheres for hig-performance anode material in lithium ion batteries[J]. Advanced Materials, 2010, 20(6): 1160-1165.

[13] Taberna P L, Mitra S, Poizot P, et al. High rate capabilities Fe_3O_4-based cu nano-architectured electrodes for lithium-ion battery applications[J]. Nature Materials, 2006, 5(7): 567-573.

[14] Mai L Q, Hu B, Chen W, et al, Lithiated MoO_3 nanobelts with greatly improved performance for lithium batteries[J]. Advanced Materials, 2007, 19(21): 3712-3716.

[15] Zhang C C, Cai X, Chen W Y, et al. 3D porous silicon/N-doped carbon composite derived from bamboo charcoal as high-performance anode material for lithium-ion batteries[J]. ACS Sustainable Chemistry & Engineering, 2018, 6(8): 9930-9939.

[16] Reddy M V, Zhang B, Kim H, et al. Highly reversible Co_3O_4/graphene hybrid anode for lithium rechargeable batteries[J]. Carbon, 2011, 49(1): 326-332.

[17] Li Y G, Tan B, Wu Y, et al. Mesoporous Co_3O_4 Nanowire arrays for lithium ion batteries with high capacity and rate capability[J]. Nano Letters, 2008, 8(1): 265-270.

[18] Peng Zheng, Wei Zhou, Yibing Wang, et al. N-doped graphene-wrapped TiO_2 nanotubes with stable surface Ti^{3+} for visible-light photocatalysis[J]. Applied Surface Science, 2020, 512: 144549.

[19] Park M S, Wang G X, Y M, et al. Preparation and electrochemical properties of SnO_2 nanowires for application in lithium-ion batteries[J]. Angewandte. Chemie International Edition, 2007, 119(5): 764-767.

[20] Kong D, Luo J, Wang Y, et al. Three-dimensional Co_3O_4@MnO_2 hierarchical nanoneedle arrays: Morphology control and electrochemical energy storage[J]. Advanced Functional Materials, 2014, 24(24): 3815-3826.

[21] Zhang L, Pu H, Zhao X, et al. Controllable synthesis of core-shell Co@CoO nanocomposites with a superior performance as an anode material for lithium-ion batteries[J]. Journal of Materials Chemistry, 2011, 21(45): 18279-18283.

[22] Ma J W, Fan H Q, Ren X H, et al. A simple absorbent cotton biotemplate to fabricate SnO_2 porous microtubules and their gas-sensing properties for chlorine[J]. ACS Sustainable Chemistry & Engineering, 2019, 7(1): 147-155.

[23] Chen Y, Wang Y, Shen X P, et al. Cyanide-metal framework derived $CoMoO_4$/Co_3O_4 hollow porous octahedrons as advanced anodes for high performance lithium ion batteries[J]. Journal of Material Chemistry A, 2017, 6(3): 1048-1056.

[24] Wang B, Li S, Wu X, et al. Self-assembly of ultrathin mesoporous $CoMoO_4$ nanosheet networks on flexible carbon fabric as a binder-free anode for lithium-ion batteries[J]. New Journal of Chemistry, 2016, 40(3): 2259-2267.

[25] Ahmed B, Shahid M, Nagaraju D, et al. Surface passivation of MoO_3 nanorods by atomic layer deposition toward high rate durable li ion battery anodes[J]. ACS Applied Materials & Inter-

faces, 2015, 7(24): 13154-13163.
[26] Chen N, Yao Y, Wang D, et al. Long life $CoMoO_4$ as a novel anode material for lithium-ion batteries[J]. ACS Appl. Mater Interfaces, 2014, 6(13): 10661-10666.
[27] Li P, Liu J, Liu Y, et al. Three-dimensional $ZnMn_2O_4$/porous carbon framework from petroleum asphalt for high performance lithium-ion battery[J]. Electrochim. Acta, 2015, 180: 164-172.
[28] Wu X, Yan P, Yang Y, et al. Mn_2CoO_4/reduced graphene oxide composite as a promising anode material for lithium-ion batteries[J]. Ceramics International, 2015, 41(3): 4080-4086.
[29] Li L, Liu X, Wang S L, et al. Influence of surface structure on the capacity and irreversible capacity loss of Sn-based anodes for lithium ion batteries[J]. ACS Sustainable Chemistry & Engineering, 2014, 2(7): 1857-1863.
[30] F Belliard, J T S. Irvine, Electrochemical performance of ball-milled ZnO-SnO_2 systems as anodes in lithium-ion battery[J]. Journal of Power Sources, 2001, 97(7): 219-222.
[31] Zhao Y, Li X, Yan B, et al. Recent developments and understanding of novel mixed transition-metal oxides as anodes in lithium ion batteries[J]. Advanced Energy Materials, 2016, 6(8): 1502175.
[32] Wang Y, Wu Y, Xing L, et al. $CoMoO_4$/Fe_2O_3 core-shell nanorods with high lithium-storage performance as the anode of lithium-ion battery[J]. Journal of Alloys & Compounds, 2016, 689: 655-661.
[33] Yu H, Guan C, Rui X, et al. Hierarchically porous three-dimensional electrodes of $CoMoO_4$ and $ZnCo_2O_4$ and their high anode performance for lithium ion batteries[J]. Nanoscale, 2014, 6(18): 10556-10561.
[34] Wang W, Qin J, Yin Z, et al. Achieving Fully Reversible Conversion in MoO_3 for Lithium Ion Batteries by Rational Introduction of $CoMoO_4$[J]. ACS Nano, 2016, 10(11): 10106.
[35] Guo J, Zhu H, Zhou S, et al. Fast and large lithium storages from $CoMoO_4$ nanorods-graphene composite[J]. Ionics, 2015, 21(10): 1-7.
[36] Xu J, Gu S, Fan L, et al. Electrospun lotus root-like $CoMoO_4$ @ graphene nanofibers as high-performance anode for lithium ion batteries[J]. Electrochim. Acta, 2016, 196: 125-130.
[37] Tian W, Liu J, Wang Y, et al. Substrate-assisted in Situ confinement pyrolysis of zeolitic imidazolate frameworks to nitrogen-doped hierarchical porous carbon nanoframes with superior lithium storage[J]. ACS Applied Materials & Interfaces, 2017, 9(49): 42845-42855.
[38] Kaneti Y V, Tang J, Salunkhe R R, et al. Nanoarchitectured design of porous materials and nanocomposites from metal-organic frameworks[J]. Advanced Materials, 2017, 29(12): 1604898.
[39] Hu C, Xiao Y, Zhao Y, et al. Highly nitrogen-doped carbon capsules: scalable preparation and high-performance applications in fuel cells and lithium ion batteries[J]. Nanoscale, 2013, 5(7): 2726-2733.
[40] Liu J Y, Liu Y, Li P, et al. Fe-N-doped porous carbon from petroleum asphalt for highly efficient oxygen reduction reaction [J]. Carbon, 2018, 126: 1-8.
[41] Li P, Liu J Y, Wang Y, et al. Synthesis of ultrathin hollow carbon shell from petroleum asphalt for high-performance anode material in lithium-ion batteries[J]. Chemical Engineering Journal, 2016, 286: 632-639.
[42] Liu Y, Li P, Wang Y, et al. A green and template recyclable approach to prepare Fe_3O_4/porous carbon from petroleum asphalt for lithium-ion batteries[J]. Journal of Alloys & Compounds, 2017, 695: 2612-2618.
[43] Wu Z S, Ren W, Wen L, et al. Graphene anchored with Co_3O_4 nanoparticles as anode of lithium ion batteries with enhanced reversible capacity and cyclic performance[J]. ACS Nano, 2010, 4(6): 3187-3194.
[44] Yao Y, Gong Y, Yang S, et al. $CoMoO_4$ nanoparticles anchored on reduced graphene oxide nanocomposites as anodes for long-life lithium-ion batteries[J]. ACS Applied Materials & Interfaces, 2014, 6(22): 20414-20422.
[45] Jasieniak J J, Treat N D, Mcneill C R, et al. Interfacial characteristics of efficient bulk heterojunction solar cells fabricated on MoO_x anode interlayers[J]. Advanced Materials, 2016, 28(20): 3944-3951.
[46] An L, Huang L, Zhou P, et al. A Self-Standing high-performance hydrogen evolution electrode with nanostructured $NiCo_2O_4$/CuS heterostructures[J]. Advanced Functional Materials, 2016, 25(43): 6814-6822.
[47] Liu X, Liu W, Ko M, et al. Metal (Ni, Co)-metal oxides/graphene nanocomposites as multifunctional electrocatalysts [J]. Advanced Functional Materials, 2015, 25(36): 5799-5808.
[48] Tian W, Hu H, Wang Y, et al. Metal-organic frameworks mediated synthesis of one-dimensional molybdenum-based/carbon composites for enhanced lithium storage[J]. ACS Nano, 2018, 12(2): 1990-2000.
[49] Chen Y, Liu B, Jiang W, et al. Coaxial three-dimensional $CoMoO_4$ nanowire arrays with conductive coating on carbon cloth for high-performance lithium ion battery anode[J]. Journal of Power Sources, 2015, 300: 132-138.
[50] Zheng C, Luo N J, Huang S P, et al. Nanocomposite of Mo_2N quantum dots@ MoO_3 @ nitrogen-doped carbon as a high-performance anode for lithium-ion batteries[J]. ACS Sustainable Chemistry & Engineering, 2019, 7(12): 10198-10206.
[51] Xu Z, Wang H, Li Z, et al. Sulfur refines MoO_2 distribution enabling improved lithium ion battery performance[J]. Journal of Physical Chemistry C, 2014, 118(32): 18387-18396.
[52] Cherian C T, Reddy M V, Haur S C, et al. Interconnected network of $CoMoO_4$ submicrometer particles as high capacity anode material for lithium ion batteries[J]. ACS Applied Materials & Interfaces, 2013, 5(3): 918-923.
[53] Wang Y X, Tian W, Wang L, et al. A tunable molten-Salt route for scalable synthesis of ultrathin amorphous carbon nanosheets as high-Pperformance anode materials for lithium-ion batteries[J]. ACS Applied Materials & Interfaces, 2018, 10(6): 5577-5585.
[54] Zhu X, Zhu Y, Murali S, et al. Nanostructured reduced graphene oxide/Fe_2O_3 composite as a high-performance anode material for lithium ion batteries[J]. ACS Nano, 2011, 5(4): 3333-3338.
[55] Zhang H J, Wang K X, Wu X Y, et al. MoO_2/Mo_2C heteronanotubes function as high-performance Li-ion battery electrode [J]. Advanced Functional Materials, 2014, 24(22): 3399-

3404.
[56] Fan L, Zhang Y, Zhang Q, et al. Graphene aerogels with anchored sub-Micrometer mulberry-like ZnO particles for high-rate and long-cycle anode materials in lithium ion batteries[J]. Small, 2016, 12(37): 5208-5216.
[57] Zheng Z, Zao Y, Zhang Q, et al. Robust erythrocyte-like Fe_2O_3@carbon with yolk-shell structures as high-performance anode for lithium ion batteries[J]. Chemical Engineering Journal, 2018, 347: 563-573.
[58] Zheng Z, Wu H H, Chen H X, et al. Fabrication and understanding of Cu_3Si-Si@carbon@graphene nanocomposites as high-performance anodes for lithium-ion batteries[J]. Nanoscale, 2018, 10(47): 22203-22214.
[59] Zhang Q, Chen H, Luo H, et al. Harnessing the concurrent reaction dynamics in active Si and Ge to achieve high performance of lithium-ion batteries[J]. Energy & Environmental Science, 2018, 11(3): 669-681.

Instructions to Authors

New Carbon Materials is a bimonthly journal published with the permission of the Ministry of Science and Technology and of the State News and Publication Agency. The journal is sponsored by the Institute of Coal Chemistry, Chinese Academy of Sciences, and is published by Science Press.

Aims and Scope

New Carbon Materials publishes research devoted to the physics, chemistry and technology of those organic substances that are precursors for producing aromatically or tetrahedrally bonded carbonaceous solids, and of the materials that may be produced from those organic precursors. These materials range from diamond and graphite through chars, semicokes, mesophase substances, carbons, carbon fibers, carbynes, fullerenes and carbon nanotubes, etc. Papers on the secondary production of new carbon and composites materials (for instance, carbon-carbon composites) from the above mentioned various carbons are also within the scope of the journal. Papers on organic substances will be considered if research has some relation to the resulting carbon materials.

Manuscript Requirements

1. *New Carbon Materials* accepts Research Paper, Short Communication and Review. The number of words in each Research Paper should be less than 6000 words. Short Communication < 3500 words. There is no maxium of words for Review.

2. Manuscript including an abstract, graphical abstract, highlight, keywords, reference list, original figures and captions, tables. Manuscripts can be written both in Chinese and English.

3. Manuscript should be accompanied with key words placed after Abstract and a short resume of first author (name, academic degree, professional position) placed in the end of 1st page of text as foot-note. Corresponding author and his (her) E-mail address should also be mentioned.

4. All illustrations, photographs, figures and tables should be on separate sheets, figure captions should be typed separately, not included on the diagram. Authors are requested to submit original photographs, which should have good contrast and intensity.

5. References should be individually numbered in the order in which they are cited in the text, and listed in numerical sequence on separate sheets at the end of the paper, typed in double spacing. Remember that "unpublished works" are not references! In the reference list, periodicals [1], books [2], multi-author books with editors [3], proceedings [4], patents [5], and thesis [6] should be cited in accordance with the following examples:

[1] Kandalkar S G, Dhawale D S, Kim C K, et al. Chemical synthesis of cobalt oxide thin film electrode for supercapacitor application[J]. Synthetic Metals, 2010, 160(11): 1299-1302.
[2] Inagaki M, Kang F Y. Carbon Materials Science and Engineering-From Fundamentals to Applications[M]. Beijing: Tsinghua University Press, 2011: 3-6.
[3] Toropov V V, Jones R, Willment T, et al. Weight and manufacturability optimization of composite aircraft components based on a genetic algorithm[P]. 6th World Congresses of Structural and Multidisciplinary Optimization, Rio de Janeiro, Brazil, 2005, 30.
[4] Yang H. Deposit, doping and photocatalytic activity of fibrous TiO_2[D]. Dalian University of Technology, 2007.
[5] Hemmert D, Shiraki K, Yokoyama T, et al. Optical diagnostics of shock waves generated by a pulsed streamer discharge in water[C]. Pulsed Power Conference, 2003. Digest of Technical Papers. PPC-2003. 14th IEEE International. IEEE, 2003, 1: 232-235.

Note: For the references with more than three authors, please give the first three and mark "et al".

6. Publication of papers in the journal is free of charge.

7. Manuscript Submission: Online submission: http://xxtcl.sxicc.ac.cn/EN/volumn/home.shtml